Polarized neutron reflectometer: A new instrument to measure magnetic depth profiles

G. P. Felcher, R. O. Hilleke, R. K. Crawford, J. Haumann, R. Kleb, and G. Ostrowski

Argonne National Laboratory, Argonne, Illinois 60439

A description is given of the prototype polarized neutron reflectometer installed at the intense pulsed neutron source. This instrument is designed for determining the magnetic depth profiles near the surfaces of ferromagnets and superconductors, by measuring the spin-dependent reflectivities of a well-collimated (0.01°) beam of cold neutrons from surfaces of a few cm^2. Magnetic profiles can be determined with the spatial resolution of 40 Å, over thicknesses up to 5000 Å. Variations of the magnetic flux of the order of 10^{-5} G cm^2 can be detected.

INTRODUCTION

X-ray reflection has been extensively used to determine the density profiles close to the surfaces of materials.[1] The refractive index for x rays in materials is[2]

$$n = 1 - (\lambda^2 e^2/2\pi mc^2)(Z/V) , \qquad (1)$$

where λ is the x-ray wavelength and Z/V (basically a scattering amplitude) represents the number of electrons per unit volume. In view of Snell's law,[3] a refractive index less than unity means that for a given wavelength there is always a critical angle below which the reflectivity is total. For larger angles, the x rays partially penetrate the surface and, if the material is stratified in layers of different n, partial reflection occurs also at each interface. Hence, the observed reflectivity above the critical angle is directly related to the thickness and the refractive index of the succession of strata of which the material is made.

The information that neutrons can provide is in principle parallel to that obtained by x rays. Here we have both a nuclear and a magnetic scattering amplitude. The nuclear amplitudes can be quite different even for adjacent elements (in contrast with the x-ray case), or even for different isotopes of a single element. Thus the contrast between layers may be considerably larger than for x rays, or could be made larger by appropriate isotopic substitution[4–8] (notably light with heavy hydrogen). Neutrons are also scattered by magnetic moments and the refractive index at a depth z from the surface is proportional to the local magnetic induction $\mathbf{B}(z)$. The magnetic term in the refractive index[9,10] has a sign, which depends on the relative orientation of $\mathbf{B}$ with the neutron spin. The scope of the present paper is to present in more detail the treatment of the neutron reflectivity, and then to show the way in which the polarized neutron reflectometer was conceived, constructed, and tested to the point of becoming a useful tool for the determination of magnetic depth profiles in superconductors and ferromagnets.[11–14]

I. NEUTRON REFLECTIVITY

In a stratified material the interaction potential varies only as a function of the depth from the surface z (no lateral fluctuations). The incident, transmitted, and reflected beams are plane waves defined by their momenta, and the interaction potential affects only their component normal to the surface: thus the calculation of the reflectivity reduces to the well-known problem of a particle in a one-dimensional potential box.[15]

The interaction potential in the atomic volume V contains a nuclear part, defined as $(2\pi\hbar^2/m)(b/V)$, the nuclear scattering amplitude per unit volume, and a magnetic part $\boldsymbol{\mu}_n \cdot \mathbf{B}$, where $\mathbf{B}$ is the magnetic induction (m is the neutron mass, μ_n its magnetic moment, and b the nuclear scattering amplitude of the atom contained in V). Across the surface there is no discontinuity of $\mathbf{B}_z$ (the component of $\mathbf{B}$ normal to the surface), which means that if the sample is magnetized perpendicularly to the surface there is no magnetic effect in the neutron reflectivity. Rather than considering the general case, we restrict the neutron polarization and $\mathbf{B}$ to the plane of the surface. We can define two components, $\mathbf{B}_{\parallel}$ and $\mathbf{B}_{\perp}$, respectively, parallel and normal to the neutron quantization axis, defined by an external magnetic field $\mathbf{H}$. The overall geometry is illustrated in Fig. 1. Notice that in reality the parallel component of the induction gives rise to an interaction potential of the form $\mu_n \cdot (\mathbf{B}_{\parallel} - \mathbf{H})$: in a diamagnetic material (for example, a superconductor) the neutrons see a negative magnetic field.

The two spinor components $f_+(z)$, $f_-(z)$ of the neutron wave function obey, at a depth z in the medium, the Schroedinger equations
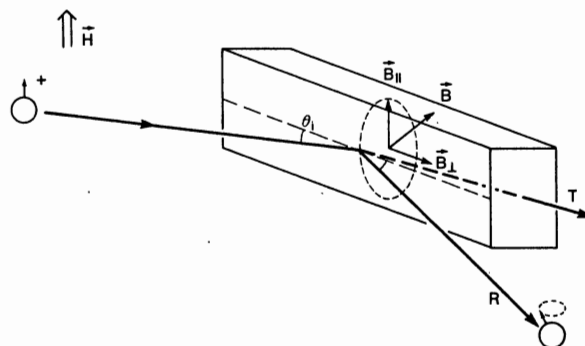

FIG. 1. Scheme of the reflection geometry of a polarized neutron beam, including the reflected (R) and refracted (T) beams. The neutrons are initially polarized in the external magnetic field $\mathbf{H}_0$. If the magnetic field in the sample $\mathbf{B}$ has a component perpendicular to $\mathbf{H}_0$, the exit beams are partially depolarized.

$$f''_+ + [k_z^2 - 4\pi(b/V + cB_\parallel)]f_+ - 4\pi cB_\perp f_- = 0,$$
$$f''_- + [k_z^2 - 4\pi(b/V - cB_\parallel)]f_- - 4\pi cB_\perp f_+ = 0, \quad (2)$$

where $k_z = 2\pi(\sin\theta_i/\lambda)$ is the component of the momen-

tum of the incident neutron normal to the surface, θ_i the angle of incidence, λ the neutron wavelength, and $c = 2\pi m\mu/h^2$. In a region of z in which both b/V and $\mathbf{B}$ are constant the solutions of the Eqs. (2) are

$$f_+ = A_1 \exp(ik_+ z) + A_2 \exp(-ik_+ z) + A_3 \exp(ik_- z) + A_4 \exp(-ik_- z)$$

$$f_- = A_1 \frac{B_\parallel - B_T}{B_\perp} \exp(ik_+ z) + A_2 \frac{B_\parallel - B_T}{B_\perp} \exp(-ik_+ z)$$

$$+ A_3 \frac{B_T + B_\parallel}{B_\perp} \exp(ik_- z) + A_4 \frac{B_T + B_\parallel}{B_\perp} \exp(-ik_- z), \quad (3)$$

where

$$B_T = \sqrt{B_\parallel^2 + B_\perp^2}$$

and

$$k_\pm = \sqrt{k_z^2 - 4\pi(b/V \pm cB_T)}. \quad (4)$$

The normal component of the neutron momentum in the vacuum is modified in the medium to $k_\pm$, as if the medium had refractive indices

$$n_\pm = 1 - (\lambda^2/2\pi)(b/V \pm cB_T). \quad (5)$$

The coefficients A_i are determined by imposing the condition that the wavefunctions and their derivatives are continuous at the boundaries of one region of constant potential. One such boundary is the material/vacuum interface. Calling χ_+ and χ_- the wavefunctions in the vacuum space, the wavefunctions at a depth z from the surface are

$$\begin{vmatrix} f_+(z) \\ f'_+(z) \\ f_-(z) \\ f'_-(z) \end{vmatrix} = \begin{vmatrix} a_{11} & a_{12} & a_{13} & a_{14} \\ a_{21} & a_{11} & a_{23} & a_{13} \\ a_{13} & a_{14} & a_{33} & a_{34} \\ a_{23} & a_{13} & a_{43} & a_{33} \end{vmatrix} \cdot \begin{vmatrix} \chi_+(0) \\ \chi'_+(0) \\ \chi_-(0) \\ \chi'_-(0) \end{vmatrix} \quad (6)$$

with the matrix elements a_{ij} given in Table I.

    If in the material the refractive index varies as a function of depth, we represent the function $n(z)$ with a histogram of n layers of constant refractive indices,[16] at the depths $z_1,...,z_n$. Equation (6) shows that progressing from the surface the wavefunction at z_1 can be calculated, and this becomes the new base function to calculate z_2 and so on. The resulting matrix at z_n is simply the product of the n matrices of the individual layers in their sequence. While certainly this product can always be calculated numerically, its analytical form may be quite complex.[17]

    Suppose that at depth greater than z_n the refractive index becomes constant. Then the reflectances R and the transmittances T can be calculated by explicitly writing the wave functions at z_n and at the surface. Assuming for instance that the incident neutrons are polarized in the (+) state

$$f_+(z_n) = T_{++} \exp ik_{+,n} z_n;$$
$$\chi_+(z<0) = \exp ik_z z + R_{++} \exp -ik_z z,$$
$$f_-(z_n) = T_{+-} \exp ik_{-,n} z_n;$$
$$\chi_-(z<0) = R_{+-} \exp -ik_z z, \quad (7)$$

where the notations T_{+-}, etc., indicate that the spin state of the incident neutron is (+), and that of the transmitted (or reflected) neutron is (−). Equation (6) now allows the determination of $R_{++}, R_{+-}, T_{++}, T_{+-}$, and of the reflectivities $|R_{++}|^2$ and $|R_{+-}|^2$.

    It is worthwhile to present the explicit solutions for some simple cases. Suppose that the material is homogeneous, or that both b/V and $\mathbf{B}$ are constant. Also, we take $B_\perp = 0$: the equations for the two spin states are now decoupled, and the reflectances are

$$R_{\pm\pm} = \frac{k_z - k_\pm}{k_z + k_\pm}. \quad (8)$$

For each spin state we have now the standard optical form of the reflectivity. For instance, for fixed angle of incidence the reflectivities are

TABLE I. Elements of the reflection matrix [Eq. (6)].

$$a_{11} = a_{22} = \frac{B_T + B_\parallel}{2 B_T}\cos k_+ z + \frac{B_T - B_\parallel}{2 B_T}\cos k_- z$$

$$a_{12} = \frac{B_T + B_\parallel}{2 k_+ B_T}\sin k_+ z + \frac{B_T - B_\parallel}{2 k_- B_T}\sin k_- z$$

$$a_{13} = a_{24} = a_{31} = a_{42} = \frac{B_\perp}{2 B_T}(\cos k_+ z - \cos k_- z)$$

$$a_{14} = a_{32} = \frac{B_\perp}{2 B_T}\left(\frac{1}{k_+}\sin k_+ z - \frac{1}{k_-}\sin k_- z\right)$$

$$a_{21} = -k_+ \frac{B_T + B_\parallel}{2 B_T}\sin k_+ z - k_- \frac{B_T - B_\parallel}{2 B_T}\sin k_- z$$

$$a_{23} = a_{41} = \frac{B_\perp}{2 B_T}(-k_+ \sin k_+ z + k_- \sin k_- z)$$

$$a_{33} = a_{44} = \frac{B_T - B_\parallel}{2 B_T}\cos k_+ z + \frac{B_T + B_\parallel}{2 B_T}\cos k_- z$$

$$a_{34} = \frac{B_T - B_\parallel}{2 k_+ B_T}\sin k_+ z + \frac{B_T + B_\parallel}{2 k_- B_T}\sin k_- z$$

$$a_{43} = -k_+ \frac{B_T - B_\parallel}{2 B_T}\sin k_+ z - k_- \frac{B_T + B_\parallel}{2 B_T}\sin k_- z$$

$$|R_{\pm\pm}|^2$$

$$= \left| \frac{\sin\theta_i - \sqrt{\sin^2\theta_i - (\lambda^2/\pi)(b/V \pm cB_\parallel)}}{\sin\theta_i + \sqrt{\sin^2\theta_i - (\lambda^2/\pi)(b/V \pm cB_\parallel)}} \right|^2 . \tag{9}$$

Both functions monotonically increase with wavelengths up to $\lambda_{\pm c}$, where they become unity. Moreover, the two reflectivities have identical form, and can be superimposed by rescaling the wavelengths

$$\lambda_+ \sqrt{b/V + cB_\parallel} = \lambda_- \sqrt{b/V - cB_\parallel} . \tag{10}$$

These relations show how it is possible, from an experimental spectrum, to easily check if indeed the magnetic induction **B** in a material is constant, and to determine its absolute magnitude.

The evaluation of the magnetic terms when **B** is not along the quantization axis is more complex. If $\mathbf{B}_\parallel = 0$ and $\mathbf{B}_\perp$ is constant, the reflectances of an initially polarized (+) beam are

$$R_{\substack{++ \\ +-}} = \frac{1}{2}\left(\frac{k_z - k_+}{k_z + k_+} \pm \frac{k_z - k_-}{k_z + k_-} \right). \tag{11}$$

In this case R_{++} is never unity; however, the sum of the reflectivities becomes equal to one for $k_- = 0$ or $k_z^2 = 4\pi(b/V - cB_\perp)$. For a general magnetic profile, the reflectivities cannot be expressed in a closed analytical form, and they have to be calculated numerically. This means that the evaluation of the magnetic profile from the experimental reflectivities can take place only by nonlinear least-square methods. However, approximate analytical solutions have been developed which,[17] although valid only in limited regions of the reflectivity, have been helpful in providing a guidance to the solution of the problem.

II. CONCEPTUAL DESIGN

The neutron reflectivity from a given material is a function only of $k_z = 2\pi\sin\theta_i/\lambda$, the component of the neutron momentum normal to the surface. For ease of measurement it would be convenient to choose a sizeable angle of incidence; however, the choice of the wavelength is restricted by the emission spectrum of the neutron source. Even neutrons slowed down in a cold moderator have a thermal spectrum peaked around $\lambda \sim 5$ Å. At this wavelength, the critical angle is typically a fraction of degree; thus quite tight collimation of the neutron beam is required.

In principle, we have the choice of determining the reflectivity either by choosing a wavelength (monochromatizing the beam) and then measuring the reflectivity for a sequence of angles θ_i; or alternatively by pulsing the beam and measuring at fixed angle the reflectivity as a function of the neutron wavelengths, which are sorted out by time of flight between the chopper and the detector. The latter method is preferred for several reasons. It makes unnecessary the construction of very delicate rotation mechanisms. Slowly varying experimental conditions are fairly well averaged in the repeated time-of-flight measurements, rather than causing distortions of the profile. Finally, the time-of-flight method allows better matching of the angular resolution with the wavelength resolution.

In a typical reflection experiment we have $\theta_i = 0.5 \pm 0.01°$ and we want a matching wavelength resolution ($\Delta\lambda/\lambda \sim \Delta\theta/\theta$). This is not easily obtainable if the beam is monochromatized by Bragg diffraction. For a single crystal with a diffraction angle of 20°, an angular spread of 0.01° is obtained only if the monochromatizing crystal is quite perfect; but then the range of diffracted wavelengths is extremely narrow, hence the neutron intensity is low. On the other hand, a broad mosaic crystal (such that $\Delta\lambda/\lambda \sim 0.02$) would require a wide neutron beam before the monochromator, and a drastic collimation after it. In the pulsed mode, wavelength and angular resolutions are totally uncoupled; the former being defined by the characteristics of the chopper and by the chopper-detector distance; the latter by a gradual system of collimators from the source to the sample.

The layout of the prototype instrument, installed at the intense pulsed neutron source (IPNS) at Argonne, is illustrated in Fig. 2 (top view). Here the pulsing of the beam is provided by the source itself, which delivers 30 bursts/s of neutrons thermalized in a solid methane moderator. The neutron beam is then filtered of its high energy tail by passing it through a cold beryllium filter. The beam is progressively collimated by a series of narrow slits before arriving on the sample at grazing incidence. The beam reflected from the sample then strikes a two-dimensional position-sensitive detector. All the neutron wavelengths, beyond the Be cutoff, are utilized; the wavelengths are sorted out by time of flight. This means that the entire reflectivity curve is measured, at fixed angle of incidence, for each neutron burst; and the experiment consists of summing up the results for subsequent bursts until the desired statistical accuracy is obtained. A good spectrum requires approximately one day of operation.
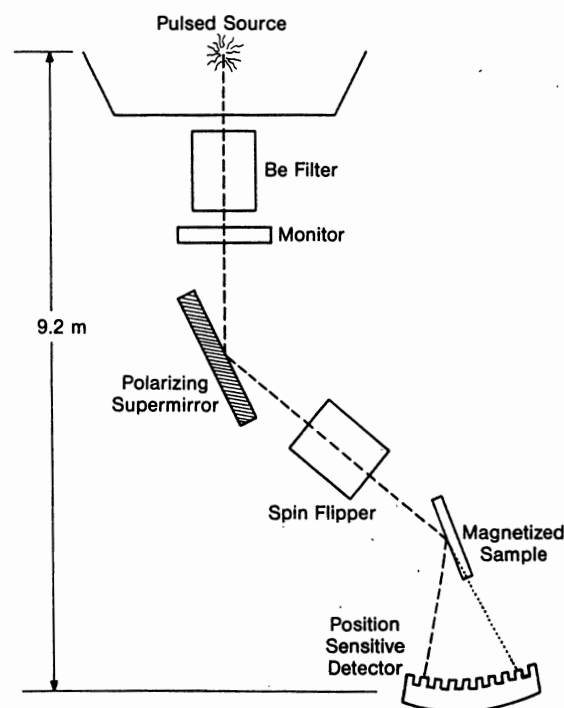

FIG. 2. Layout of the polarized neutron reflectometer.

Figure 2 illustrates some features that are required for the selection and handling of the neutron polarization. The first component is a supermirror,[18] set after the filter. This reflects only neutrons polarized parallel to the mirror magnetization, which points normally out of the page in Fig. 2. A second but important function of the mirror is to limit even further the contamination by fast neutrons, since after this reflection the beamline does not directly view the source. After the mirror, the neutrons are kept polarized by guide fields along their path. These fields could be along the original direction of the magnetization of the mirror or they could slowly vary to a different direction, depending upon the requirements of the experiment. The only constraint is that the change be sufficiently gradual that the neutron spin can follow the variation of its quantization axis. In this way, measurements can be taken with the neutron beam in one spin state (parallel to the quantization axis or $+$). Subsequently, it is desirable to obtain measurements for the opposite neutron spin state ($-$); this is obtained by energizing the neutron spin flipper inserted in the neutron path.

In the present instrument neutrons are reflected in the horizontal plane by vertically positioned magnetic surfaces. This arrangement has the advantage of being simple, quite convenient, and the mechanical construction allows easy insertion of sophisticated sample environments. However, such geometry does not allow the study of density profiles close to the surface of liquid solutions, an area of research which presently is attracting considerable interest.[8,10]

III. TECHNICAL COMPONENTS

A. Beamline

At IPNS the neutrons are produced by irradiating a target of depleted uranium with a current of 15 μA of protons accelerated to 450 MeV. The neutrons are produced in the target as a result of spallation and fast-fission processes, and are slowed down in a cold moderator of solid methane, kept at a temperature of 10 K. The emitted neutron spectrum has a Maxwellian distribution, with an effective temperature of 20 K, except for a hot tail of imperfectly moderated neutrons. The thicker the moderator, the more truly thermalized is the neutron spectrum; however, in so doing, the neutron pulse width broadens to unacceptable values. A compromise was reached by building a grooved moderator, made of alternate portions (each 1 cm high) in which the moderator is, respectively, 4 and 8 cm thick.[19] The pulse width in this case is 160 μs, and the shape of the pulse had a very sharp rise followed by a slow decay. This pulse width was determined for a wavelength of 6 Å by measuring the time structure of a Bragg peak of mica set in back-reflection geometry. The pulse width increases slightly with wavelength.

The neutron beam is filtered of its hot tail by passing through 15 cm of beryllium at 78 K; Fig. 3 shows a typical filtered spectrum. The well-defined edges, due to the diffraction limits of the (002) and (101) reflections, allow an easy calibration of the time of flight in terms of the wavelength. The beryllium filter is quite efficient in eliminating unwanted neutrons, which are scattered by the filter and mostly absorbed in its 30-cm-thick casing of borated polyethylene.
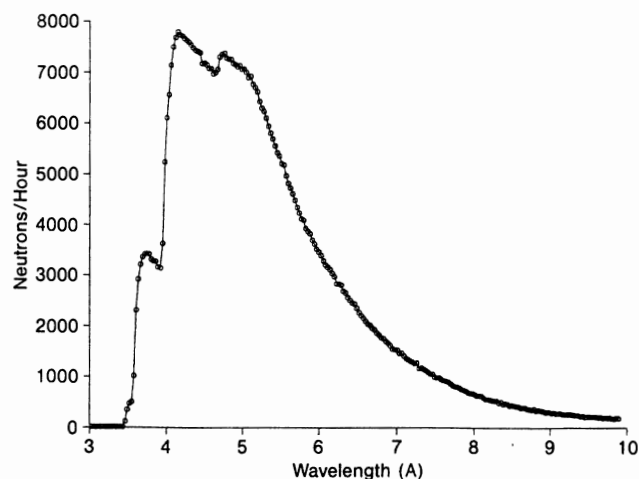

FIG. 3. The spectrum of the polarized neutron beam incident on the sample. The two edges (from left) correspond to the limits for the (002) and (100) reflections of the beryllium filter; the notch at longer wavelengths is caused by the aluminum cryostat of the methane moderator.

Unfortunately, the beryllium blocks are formed by sintering grains of sufficiently small size to cause a significant amount of small angle scattering. While these scattered neutrons are mostly blocked by a series of slits, the optical resolution of the beamline is degraded and there is a progressive loss of neutrons at longer wavelengths.

From the beryllium filter to the sample the neutrons do not have to cross any other solid barrier (except for two Mylar windows, 25 μ thick, which seal the helium-filled volume of the neutron path). Even the monitor (a pencil ^{3}He detector, covered with cadmium except for a pinhole) is in the penumbra of the beam. The beam is gradually collimated and reduced in size from the moderator (at which point the open beam channel has an area of 10×10 cm) to an exit window after the flipper (which has an aperture of 0.5×20 mm). The total flight path between the moderator and this window is 7.8 m, of which 5.6 correspond to the distance between the moderator and the filter. The collimation inside the monolith is obtained by a set of two collimators made of steel and evacuated. The walls of the neutron path after the polarizers are entirely made of blocks of lead and of ^{6}Li. The final collimating slits are also made of ^{6}Li, in order to minimize gamma production to which the detector is sensitive.

Up to now we have assumed a one-to-one correspondence between the time-of-flight and the wavelength spectra. However, in each time frame there is contamination of other wavelengths. The slower neutrons of one pulse are recorded at the same time as faster neutrons of subsequent pulses (frame overlap). With a source-detector distance of approximately 10 m and a frequency of 30 bursts/s, the first overlap takes place for neutron wavelengths of 13 Å (with the present setup, most of these neutrons are scattered away by the beryllium filter). A second cause of contamination is the presence of delayed neutrons produced in the uranium target, which, with a time constant of the order of a second, constitutes a practically uniform background. For the present target of depleted uranium the delayed neutrons amount to only 0.5% of the flux. However, this target will shortly be substituted with one of enriched uranium. This is expected

to boost the neutron production by a factor of 3, but would also emit a considerably higher percentage of delayed neutrons.

B. Polarization handling

Because we wanted a beam of polarized neutrons having a wide range of wavelengths, we decided to use a magnetic mirror to polarize the neutrons. A magnetized mirror reflects, for fixed θ_i, neutrons of one spin state of all wavelengths $\lambda > \lambda_{+c}$ and neutrons of the opposite spin state for $\lambda > \lambda_{-c}$. Hence, the mirror is a low-pass filter and a polarizer for $\lambda_{-c} > \lambda > \lambda_{+c}$. Compared with other methods of polarization, the mirror technique is the most suited for the present experimental setup because of its simplicity: the major restrictions for a general use (long wavelengths, narrow beam) are not important here.

The mirror presently in use is in reality a supermirror, made of a preordered sequence of suitable magnetic and nonmagnetic layers, with thicknesses chosen to provide a continuum of high reflectivity well beyond the critical angle of the individual component. The supermirror presently in use[18] is a composite of iron and silver layers vapor deposited on a 5×30-cm float glass substrate. When inserted in the neutron beam at an angle of 0.6°, it reflects almost completely neutrons of wavelength larger than 4 Å, with a polarization efficiency of 95% for up to 8-Å neutrons. The supermirror is suspended, with micrometric orientation adjustments, between the pole pieces of an H-shaped permanent magnet providing a field of 250 Oe.

The neutron spin flipper is of a nonadiabatic kind,[20] which flips the spins irrespective of their wavelength (and their time of arrival). Basically, it consists of two coils energized with aiding currents (nonspin-flip) or opposite currents (spin-flip). Its design follows closely that reported in the literature, and its operation is diagrammatically represented in Figs. 4(a) and 4(b). The two coils are 37 cm apart and have a diameter of 15 cm. The coil current is 3 A, providing a magnetic field of 50 Oe at the center of the coils. The flipping efficiency, for a neutron beam of dimensions 1×20 mm, is close to 100% (the present setup did not allow the duplication of systematic tests such as those reported in the literature).

Common practice in polarized neutron research suggests that the alternation of the measurements flipper on/ flipper off should take place at a frequency higher than the plausible drifts of the experimental conditions. Yet, the data collection time for the two spin states should be such that the two intensities are recorded with the same statistical error. The latter feature could have been obtained by computer controlling the switching process, but that would have slowed the operation considerably. Hence, it is preferred to switch the current in one of the two coils for every neutron pulse, or 30 times a second. The switching is ordered by a pulse from the accelerator (signaling the arrival of the proton beam on the uranium target) to a bipolar Kepco power supply; the transient is completed in less than a millisecond, well below the time of arrival of the filtered neutrons.

Rigidly attached to the flipper are the magnets providing the guide fields, which keep the neutrons polarized along their path, and the beamline itself. The whole assembly sits on a leveled table, and can be positioned by two sets of micrometric screws.

A proper handling of the neutron spin can also be used to improve the characteristics of the neutron beam. For instance, a neutron monochromator has been proposed,[21] consisting of a spin polarizer, a Drabkin flipper, and spin analyzer. The function of the Drabkin flipper is to reverse the neutron spins only for a selected wavelength,[22] with a resolution that can be made better than 1%; the unflipped neutrons are eliminated from the beam by the analyzer. A device of this kind is currently under testing: in its final arrangement, the Drabkin flipper will be automatically readjusted to reverse the neutron spins for the wavelength expected at each moment during the pulse cycle. In this way "wrong" neutrons such as delayed neutrons and those due to frame overlap, will be eliminated; the shape of the pulse will also be made sharper by the resolution function of the flipper.

C. Sample environment

The samples, with surface sizes of the order of a few cm², are set on a table which provides accurate rotation (vertical axis) and translation (perpendicular to the neutron beam). The center of the table is at 43 cm from the exit collimator. The sample positioning is checked with the aid of a permanently mounted laser installation. The laser light is reflected by a mirror which can be moved in and out of the neutron beam (at the exit of the filter) by a worm micrometer. This light passes through the same system of slits as the neutron beam before arriving at the sample. This provides easy visual observation of the illumination of the sample surface, the angle of reflection, and even gives an approximate indication of the quality of the reflecting surface.

The sample environment is very easily changed. In the most simple arrangement the spin-dependent reflectivity of ferromagnetic samples is measured in air at room temperature. This requires only a magnetic field capable of saturating the sample; the remanent magnetization can be measured in a bias as low as 2 Oe (this is needed to keep the neutrons polarized). The magnetic surfaces used in most of these experiments were protected from oxidation with a thin coating of nonmagnetic, nonreactive material such as tantalum or gold. For the study of clean exposed magnetic surfaces, an ultrahigh-vacuum chamber (10^{-11} Torr) is now
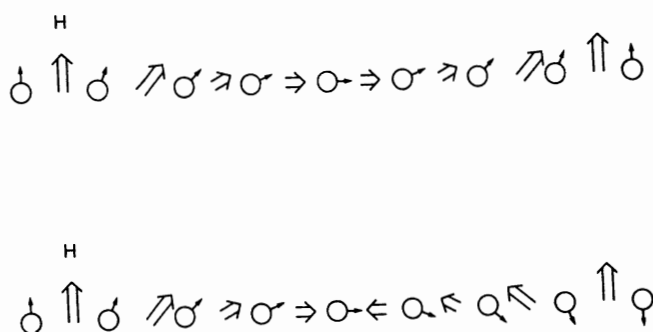

FIG. 4. The sequence of the magnetic fields and the spin polarization in the neutron spin flipper. Above: aiding currents (the neutrons are not flipped). Below: opposite currents (the neutrons are flipped).

being readied. This is at present equipped with Auger and ion guns and will later be modified to include furnaces for *in situ* perparation of the samples. For low-temperature experiments, a helium-temperature cryostat was used, equipped with a superconducting magnet.

D. Detector

Reflectivity measurements can be carried out by using a single detector, in front of which is placed a narrow slit to define the neutron acceptance. With a typical incidence angle $\theta_i = 0.5°$, a detector placed at the distance of 1 m from the sample sees the incident and the reflected beams 2 cm apart, hence the two beams can be easily discriminated. However, this method (used in an earlier version of this instrument) offers several disadvantages. The alignment with neutrons is time consuming, and proper care must be exercised to assure the acceptance of the full reflected beam (this width depends on the flatness of the sample surface). Even so, it is easy to overlook parts of the "full picture" of the reflection process, a picture that can be obtained by an area detector. In order to keep the sample/detector distance relatively short, we looked for a detector with the highest possible spatial resolution, even at the expense of its size.

The position-sensitive X–Y–time detector we use is based on a commercial microchannel-plate detector with integral photocathode and resistive anode readout.[23] The sensitive area of this detector is circular with a diameter of 25 mm. This detector is supplied with digital encoding electronics to provide a digitized X–Y output with 8 bits for X and 8 bits for Y.

This detector was converted to a neutron detector by the addition of a lithium glass scintillator, in the form of a 0.5-mm-thick disk, 25 mm in diameter.[23] Basically, the scintillator converts neutrons into light (with an estimated efficiency of 85% for 4-Å neutrons), the illuminated photocathode emits electrons which cascade in the multichannel plate, and the resulting current is recorded in the X–Y resistive anode (see Fig. 5). The operation of a detector of this type for neutron imaging has been described in detail by Schrack.[24] Different kinds of optical coupling between the scintillator and the photocathode were tried. On one hand, a good coupling assures that the maximum number of photons produced by the neutrons are accepted, and this helps in discriminating the neutron signal from the dark current and the gamma radiation. On the other hand, strong coupling means a poorer image resolution. The best compromise was found in the geometry depicted in Fig. 5. The scintillator used was polished on both sides, and it was covered on the back by diffusing alumina powder, while it was decoupled from the glass enclosing the photocathode by a Mylar ring 0.025 mm thick. In this case, with an operating voltage on the multichannel plate of 2080 V, the neutron signal was well separated from the background. Further improvement was obtained by inserting an amplitude discriminator in the commercial amplifier system. A typical neutron image of the reflected and the transmitted beams is shown in Fig. 6. In all cases, it was found that the transversal resolution of the beam was not superior to 2 mm (full width at half-maximum). This resolution, adequate but rather disappointing,
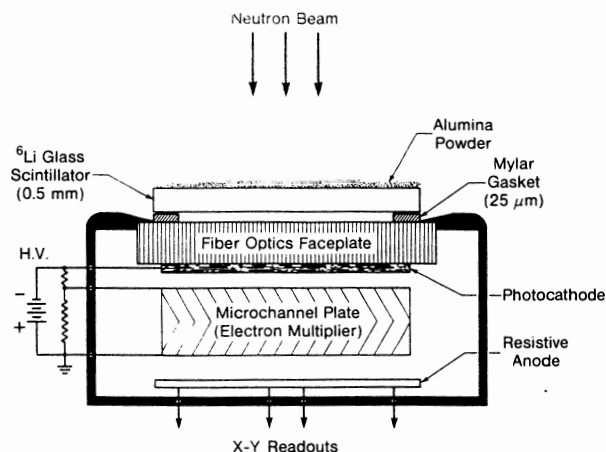

FIG. 5. Scheme of the microchannel plate, as used to detect neutrons. The neutrons are absorbed in the ^{6}Li scintillator, emitting a burst of light. The illuminated photocathode emits electrons, which are multiplied in the multichannel plate, and the resulting current is recorded in the X–Y sensitive anode. The drawing is not to scale; the thicknesses of the components, if relevant, are indicated in the headings.

may possibly be improved by inserting the scintillator in the multichannel assembly, in direct contact with the photocathode. In view of the weak neutron fluxes available, no corrections are needed for the deadtime of the counter (8 μs).

Since the scintillator has appreciable gamma sensitivity, all neutron shielding immediately surrounding the detector was made of 30-mm-thick lithium carbonate enriched with ^{6}Li, which produces no gammas upon absorption of neutrons. Surrounding this primary shielding was a shroud of 25-mm-thick lead, and around it a layer of unborated polyethylene for a thickness of 10 cm. The detector assembly was placed on a table which provided accurate translation parallel to the incident beam Z, transversal to it in the horizontal
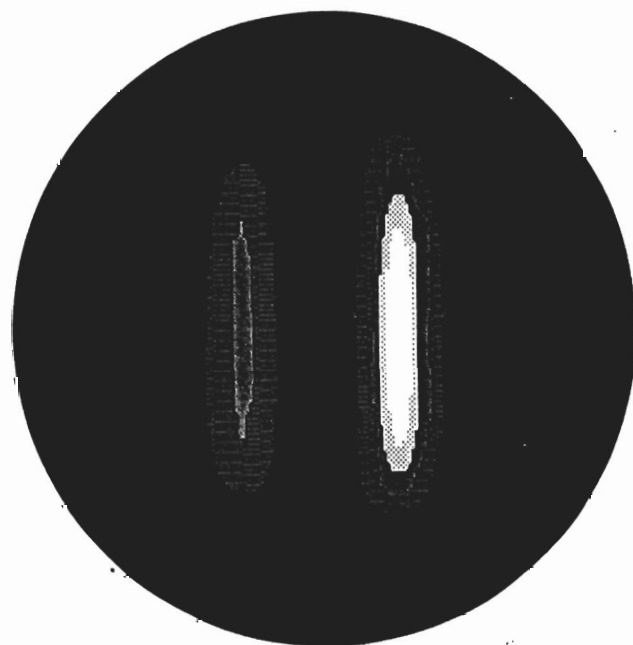

FIG. 6. Microchannel picture of the transmitted and the reflected beam from a thin film of permalloy deposited on silicon. The transmitted beam is at the right. The diameter of the circle is 25 mm. The intensities pictured here are integrated over time (or neutron wavelength).

plane X, and in the vertical direction Y. The Z motion permits the detector to be positioned at distances from the sample ranging from 60 to 120 cm, allowing measurements with different angular resolution. On the front side of the detector, a console allows the insertion of a polarization analyzer to test the polarization of the incident or the reflected beams. The transversal motions (each of which has a 10-cm range) allow exploration of different regions of the scattering space with this rather small area detector.

The commercial electronics supplied with the detector have been modified to extract a timing pulse to use for neutron time-of-flight encoding. This timing pulse and the digital X–Y data are routed through interface modules which function as a line driver for transmission of signals over a distance (about 40 m) to the data-acquisition system. These interface modules allow the option of substituting the state of the polarization flipper in place of the least-significant bit of the Y data.

E. Data-acquisition system

A standard IPNS front-end data-acquisition system[25,26] is used to time encode the signals from the area detector interface and from the beam monitor, and to histogram the resulting time-of-flight data. Figure 7 shows a schematic layout of this system. A "clock module" provides an 8-MHz clocking signal utilized by all the time-of-flight encoding modules in the system. The time-of-flight encoding module used for area detectors scales this 8-MHz signal to a 1-MHz signal, which is applied to a counter in this module. The clock module zeros this counter at the time the proton pulse arrives at the target, so this counter then keeps a running count of the time (in microseconds) since the last pulse of neutrons was produced. When a timing pulse is received from the area-detector interface modules, the current value in this scaler is taken as the neutron time-of-flight (16 bits), and this along with the 16 bits of X–Y data from the interface modules constitutes one neutron "event" which is loaded into a buffer. When this buffer is filled to three-fourths ca-

pacity (96 events), the buffer module signals a microprocessor which histograms the data.

A different time-encoder module in this same data-acquisition system receives the pulses resulting from events in the beam monitor detector. These pulses are used to generate a digital time of flight for these events utilizing the same 8-MHz clock signal in a manner similar to that used for the area detector, and these digitized events are stored in a separate buffer.

A microprocessor is dedicated to histogramming the events from the area detector and the beam monitor detector. When one of the time-of-flight encoder modules fills its buffer and interrupts the microprocessor, the microprocessor supervises the transfer of the data from the corresponding buffer to a buffer region in its own memory. When it is not involved in such transfers, the microprocessor processes the data from this latter buffer region to form a time-of-flight histogram for the beam monitor and an X–Y time histogram for the area detector. These histograms are formed in the microprocessor system memory, which allows up to 1 Mbyte (expandable to 4 Mbytes) of histogram space. The histogramming is under complete software control, so it is possible to individually select the range of time-of-flight values to be included in each time slice in the area-detector histogram and to individually select the range of X and Y values to be included in each bin within that slice. Normal operation for this instrument involves using 240 time slices of equal time width, and combining all Y values for four adjacent X values into the same bin within a slice. This produces an X–Y–time histogram of size $64 \times 1 \times 240$. Other histogramming combinations are used for testing and calibration purposes.

When the flipper is being used, an electronic switch switches the least-significant Y bit in the data from the area detector synchronously with the flipper, to indicate the flipper state. Optionally, this switch can also be used to switch the beam monitor input synchronously with the flipper, so that the beam monitor appears to the data-acquisition system as two separate detectors. In this case, the microprocessor histogramming tables are constructed so that two sepa-
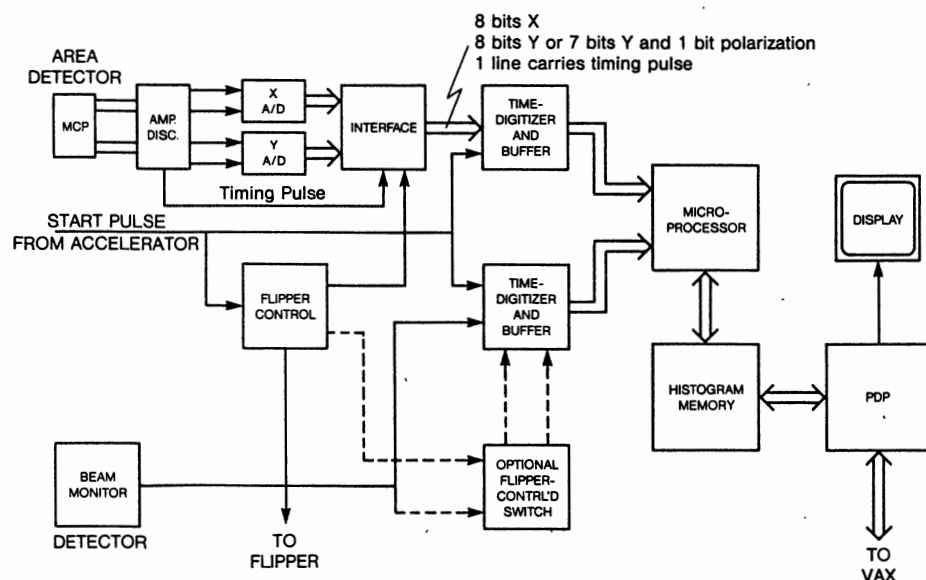

FIG. 7. Schematic representation of the data-acquisition system for the polarized neutron reflectometer.

rate area detector histograms (and optionally, two separate beam monitor histograms) are formed to correspond to the two flipper states. Since the resolution of the area detector for neutron events is only about 2 mm, discarding the least-significant encoded bit of the Y position (which corresponds to about 0.1 mm) has no appreciable effect on the overall X–Y resolution of the detector.

A minicomputer (Digital PDP-11/34A)[27] serves as the general user interface to the data-acquisition system. This computer is used to set up the histogramming tables and download them to the microprocessor system. This computer also maintains disk files for completed histogram data. A color graphics system on this computer allows the user to display live histogram data as it is being acquired or to display file data of previously acquired histograms. Both color density displays of area detector data and standard displays of beam monitor data or of particular cuts through the area detector data are available.

F. Data analysis

A DECNET-ETHERNET[27] connection allows easy transfer of completed histogram files from the PDP-11 station computer to the VAX[27] data-analysis computers for further processing. Each data set consists of three spectra: a monitor spectrum and a 64 position-channel spectrum corresponding to the channels in which the 25-mm-wide detector is subdivided horizontally for each of the two spin states. The time dimension of each spectrum consists of 240 channels, with a channel width of 50 or 80 μs depending upon the problem on hand.

The program library on the VAX allows conversion of the raw data into spin-dependent reflectivity (either in tabular or graphical form) in a matter of a few minutes. These programs include the visual display of the position-dependent intensities in a desired time slice; integration of the reflected peak and normalization to the incident beam; change of the scale from time-of-flight to neutron wavelength; and evaluation and display of the polarization function $P = (I_+ - I_-)/(I_+ + I_-)$ as a function of wavelength, for a preassigned error bar.

Other programs calculate the reflectivity for a given assembly of layers of different refractive indices according to the algorithm presented in Eq. (6). Absorption is taken into account by introducing an imaginary component in the refractive indices. The reflectivities are calculated for a given angle of incidence as a function of the neutron wavelength. The effect of the instrumental resolution, which actually is due both to the wavelength resolution and to the angular resolution, is taken into account by assuming that there is an angular spread of Gaussian form. In this way, the calculated reflectivity is compared with the experimental one. This manual procedure, however, is satisfactory only if the experimental data are used to determine one or two parameters in the magnetic profiles. More recently, the calculation of the reflectivity (without absorption) has been inserted in a nonlinear least-squares fitting program. In this program, only the refractive indices and their z dependence are allowed to vary, while the angle of incidence and the angular resolution are kept constant.

IV. NEUTRON REFLECTION TESTS

Neutron reflection measurements require good surfaces, which should be flat within a few optical fringes over an area of several square centimeters and should have mirrorlike quality. These optical requirements may ask for the development of elaborate polishing procedures, depending on the sample to be measured.

We tested the equipment with a round of fused silica[28] (5 cm diameter) of interferometric quality. The measured reflectivity, shown in Fig. 8, is in agreement with that calculated using Eq. (9). The raw data from which the reflectivity is obtained consists of a sequence of time slices of the intensities recorded by the microchannel-plate detector. A representative sample of time slices is presented in Fig. 9, where the portion of the incident beam that does not illuminate the surface, and the reflected and refracted beams are all visible. The latter beam is easily recognizable because its intensity is complementary to that of the reflected beam and its position changes with the wavelength, since the glass works as a dispersive prism.

The reflectivity curve presented in Fig. 8 required a collection time of the order of 10 h. Even with a neutron spectrum of the shape presented in Fig. 3, highest for wavelengths at which the reflectivity is low, the available intensity at present limits reliable measurements of the reflectivity to between 1 and 10^{-3}, a range which unfortunately is rather limited. The normal component of the momentum in the material varies from zero (total reflection) to approximately the value in the vacuum k_z. For a wavelength of 4 Å and angle of incidence $\theta_i = 0.5°$, $k_z = 0.013$ Å^{-1}. For this range of momenta Δk_z the resolution in thickness Δz may be defined by $2\Delta k_z \, \Delta z = 1$; numerically, $\Delta z = 40$ Å.

A second question is over what distance is it possible to observe correlation of the refractive indices. This depends on the angular resolution of the incident beam, as becomes clear by writing the reflectivity of a uniform film[16] of thickness z_0
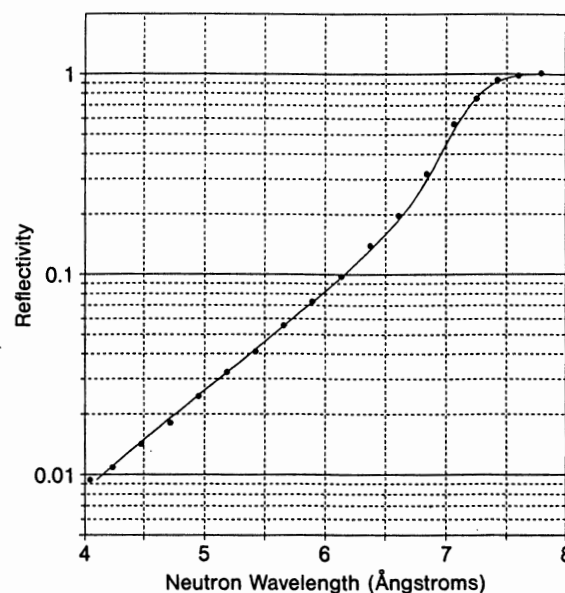

FIG. 8. Reflectivity of a silica glass surface of interferometric quality. The continuous line is calculated for an angle of incidence $\theta_i = 0.435° \pm 0.015°$.
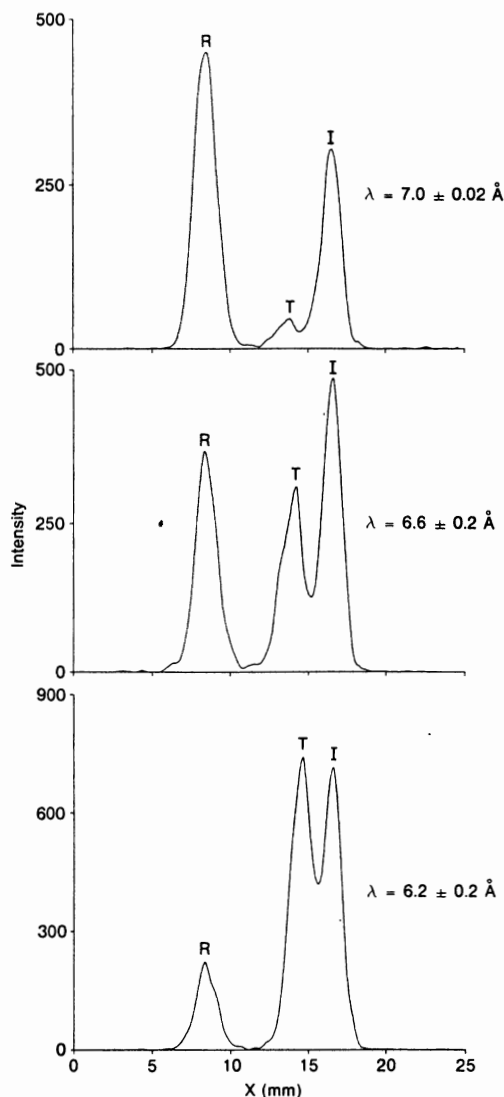
FIG. 9. The intensities recorded by the multichannel plate for silica glass (Fig. 8) as a function of the translation normal to the beam (X coordinate). Different time slices are presented; well visible are the reflected (R) and the refracted (T) beams. (I) indicates the portion of the incident beam that has not interacted with this surface.

$$|R|^2 = \frac{r_1^2 + r_2^2 + 2r_1 r_2 \cos(2k_1 z_0)}{1 + r_1^2 r_2^2 + 2r_1 r_2 \cos(2k_1 z_0)}, \quad (12)$$

where r_1 and r_2 are the reflectance at surface and the back of the film and k_1 is the normal component of the neutron momentum in the film. The divergence of the incoming beam is taken into account by integrating Eq. (12) over a corresponding range of k_1, which if large enough yields the incoherent limit

$$\overline{|R|^2} = \frac{r_1^2 + r_2^2 - 2r_1^2 r_2^2}{1 - r_1^2 r_2^2}. \quad (13)$$

With our experimental beam divergence of 0.01°, interference fringes are not observable for film thicknesses greater than 0.5 μm, at which point the reflectance of the front face and the back face of the film are decoupled and independent from the film thickness.

The above discussion is pertinent to the study of the variation of refractive index in thin films. These are obtained

by depositing the material onto a polished substrate, whose basic constraint is that its reflectivity be less than that of the covering film. Silicon single crystals were used, (111) oriented, since b/V for silicon is less than that of most substances; polished titanium slabs were also used (since the scattering amplitude of titanium is negative, this material never totally reflects neutrons).

The main difficulty in analyzing the reflectivity measurements is the presence in the samples of lateral fluctuations of the refractive index; i.e., dishomogeneities parallel to the surface. Of these, the most common is a roughness of the surface, which might appear not only in imperfectly polished samples, but even for films deposited on a smooth substrate. The effect of lateral dishomogeneities is to invalidate the one-dimensional treatment of the reflectivity; practically speaking, neutrons are subtracted from the reflected beam and scattered elsewhere.

In Fig. 10 is shown the reflectivity of a rough lead film grown on an optically flat silicon support. The reflectivity at shorter wavelengths drops much more drastically than expected. Conventionally, this effect is explained by introducing a Debye–Waller factor[29] to modify the unperturbed reflectance R_0

$$|R(k_z)|^2 = |R_0(k_z)|^2 \exp(-4k_z k_1 \langle z_D^2 \rangle), \quad (14)$$

where k_z, k_1 are the normal components of the neutron momentum in vacuum and in the material and $\langle z_D^2 \rangle^{1/2}$ is the average surface roughness. Adding this term, a good fit to the data is obtained for a surface roughness of 65 Å.

In Fig. 11 are presented, for the same sample, time slices of the small angle-scattering region. There is evidence of a sizeable amount of neutron scattering. Systematic studies have been made in the past on the diffuse scattering of x rays in similar geometry on surfaces with controlled roughness.[30]
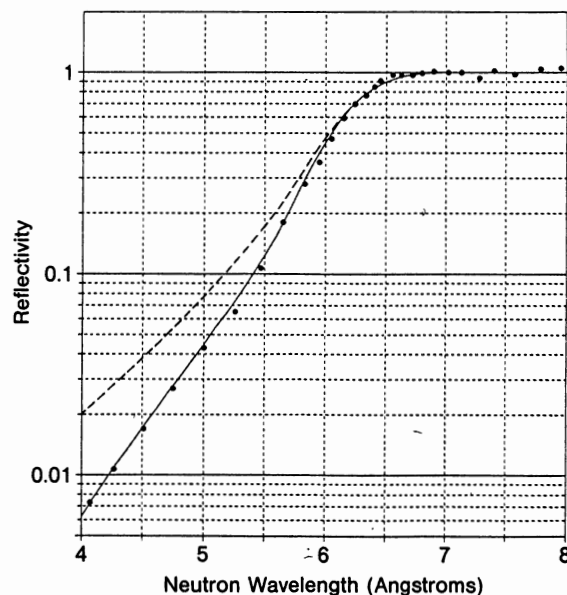

FIG. 10. The reflectivity of a film of lead, 2 μ thick, deposited on a single-crystal silicon support (111 face). Dotted line: calculated reflectivity for an angle of incidence $\theta_i = 0.355 \pm 0.020°$. Continuous line: a surface roughness of 65 Å has been added in the calculation.
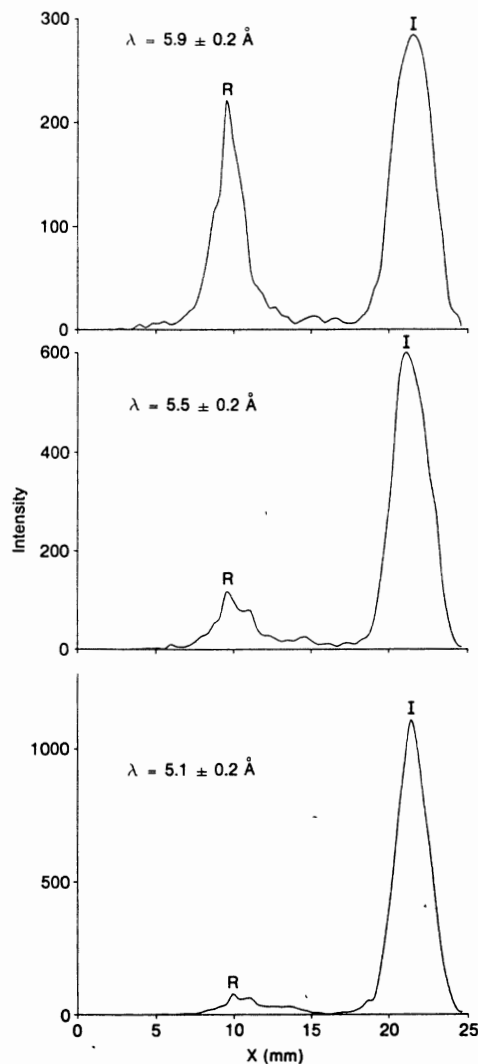
Neutron reflectometer

FIG. 11. Intensities recorded by the multichannel plate for the lead film of Fig. 10. Note the significant diffuse scattering between the incident (I) and the reflected (R) beams, particularly strong for wavelengths at which the reflectivity is low.

However, the scattered intensities have been explained only approximately in the scheme of the distorted wave first Born approximation.[31] In summary, the presence of surface roughness (and in general of lateral dishomogeneities) makes less accurate the determination of the density profiles. However, the development of an adequate scattering theory may make, in the future, the study of scattering at grazing incidence quite useful and complementary to the small angle scattering technique in the transmission geometry.

One of the novelties of the instrument described here is the use of polarized neutrons. The polarization efficiency of the instrument was tested by analyzing the polarization of the beam at the sample site with a precalibrated Fe–Ge superlattice[32] of large spacing (40 Å), which in the fundamental Bragg reflection practically diffracts only neutrons of one spin state. The incident beam was analyzed for several wavelengths and found to be 95% polarized up to 8 Å. For larger wavelengths, the polarization efficiency of the instrument degrades. However, in the geometry customarily used, at these wavelengths the surfaces totally reflect neutrons for

both spin states and, hence, strong corrections are unnecessary.

An example of spin-dependent reflectivity (from a ferromagnetic sample) is presented in Fig. 12. The sample here is a single crystal of nickel,[33] (110) face, saturated in the (111) easy direction (in the plane of the surface) by a tiny electromagnet. While this is a preliminary test, and both the magnetic circuitry and the surface flatness have still to be improved, it already shows several of the features unique to the polarized neutron reflection method.

The two reflectivity curves for neutrons polarized parallel and antiparallel to the sample magnetization allow the determination of both the magnetic and the chemical profiles. However, the latter profile can also be independently obtained either by raising the temperature above the point of magnetic order, or alternatively by applying a magnetic field normal to the surface sufficiently strong to magnetize the sample in that direction. If the direction of the magnetization in the sample is not parallel to the neutron quantization axis the reflected beam is depolarized [Eq. (11)]. This is routinely checked with the insertion of a polarization analysis leg.

The visual inspection of the $+$ and $-$ reflectivity curves already allows some conclusion on the magnetic profile. As shown in Eq. (10) for constant magnetization the two curves are identical except for a rescaling of λ. Not unexpectedly, this is the case for nickel at room temperature. Even for this relatively weak ferromagnet, the spin-dependent reflectivities show large differences. For bulk samples, magnetic profiles have been obtained[34] with a resolution of 50 G, and for thin films it has been estimated[13] that the magnetization of a ferromagnetic monolayer (0.5 μ_B/atom) should still be detectable.

The instrument described here has undergone a contin-

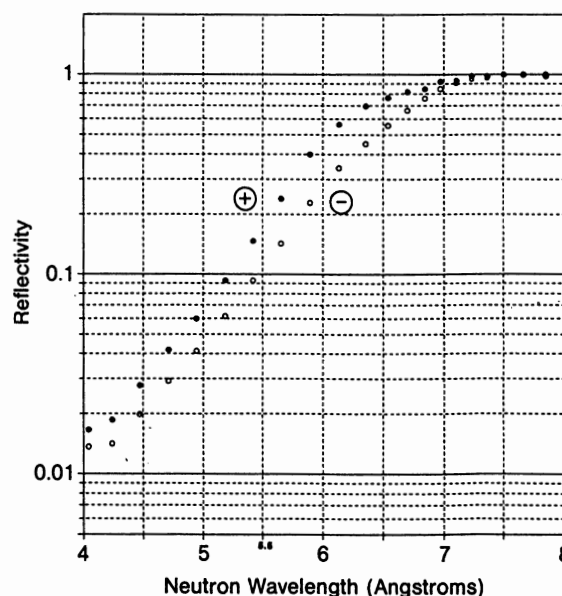FIG. 12. Preliminary reflectivity curve for a nickel single crystal with the (110) face exposed. $\theta_i \simeq 0.7°$. The spin-dependent reflectivities ($+$ and $-$) were measured with a magnetic field of 20 Oe applied in the (1$\bar{1}$1) direction.

uous evolution, making possible the solution of gradually more complex problems. Already at an early stage, the penetration depth of a magnetic field in superconducting niobium was determined.[11] Later it was used to define the magnetic profiles of films of iron oxides as a function of their oxidation state.[14] More complex profiles have recently been obtained for films of permalloy with unidirectional anisotropy.[35] The detailed shape of the penetration of a magnetic field into superconducting lead has been resolved.[34] Its potential applications are far from being exhausted; and, installed at a national facility, it is open for use by the scientific community at large.

ACKNOWLEDGMENTS

[1] D. H. Bilderback, Proc. SPIE Int. Soc. Opt. Eng. **315**, 90 (1981).

[2] R. W. James, *The Optical Principles of the Diffraction of X-rays* (Cornell University, Ithaca, NY, 1965).

[3] N. Born and E. Wolf, *Principles of Optics* (Pergamon, Oxford, 1975).

[4] J. B. Hayter, R. R. Highfield, B. J. Pullman, R. K. Thomas, A. I. McMullen, and J. Penfold, J. Chem. Soc. Faraday Trans. **77**, 1437 (1981).

[5] R. M. Niklow, M. Pomerantz, and A. Segmuller, Phys. Rev. B **23**, 1081 (1981).

[6] R. R. Highfield, R. P. Humes, R. K. Thomas, P. G. Cummings, D. P. Gregory, J. Mingins, J. B. Hayter, and O. Schaerpf, J. Coll. Interface Sci. **97**, 367 (1984).

[7] H. Scheckenhofer and A. Steyerl, Phys. Rev. Lett. **39**, 1310 (1977).

[8] B. Farnoux, Proceedings of the Conference "Neutron scattering in the 'nineties," IAEA, Vienna 1985, p. 205.

[9] G. P. Felcher, Phys. Rev. B **24**, 1595 (1981).

[10] J. Penfold and W. G. Williams, Rutherford-Appleton Laboratory Report RAL-85-045, 1985 (unpublished).

[11] G. P. Felcher, R. T. Kampwirth, K. E. Gray, and R. Felici, Phys. Rev. Lett. **52**, 1539 (1984).

[12] G. P. Felcher, R. Felici, R. R. Kampwirth, and K. E. Gray, J. Appl. Phys. **57**, 3789 (1985).

[13] G. P. Felcher, K. E. Gray, R. T. Kampwirth, and M. B. Brodsky, Physica **137B**, 59 (1986).

[14] S. S. P. Parkin, R. Sigsbee, R. Felici, and G. P. Felcher, Appl. Phys. Lett. **48**, 604 (1986).

[15] L. I. Schiff, *Quantum Mechanics* (McGraw-Hill, New York, 1949).

[16] See Ref. 3, p. 51.

[17] J. Jacobsson, in *Progress in Optics*, edited by E. Wolf (North Holland, Amsterdam, 1966).

[18] P. A. Degleish, J. B. Hayter, and F. Mezei, in *Neutron Spin Echo, Lecture Notes in Physics no. 128*, edited by F. Mezei (Springer, Berlin, 1980).

[19] J. M. Carpenter, A. W. Schulke, T. L. Scott, D. G. Wozniak, B. E. Benson, and B. D. Leyda, Proceedings of the Eighth Meeting of the International Collaboration on Advanced Neutron Sources (ICANS-VIII), Rutherford–Appleton Laboratory Report RAL-85-110, Vol. I, p. 311, 1985.

[20] T. J. L. Jones and W. G. Williams, Nucl. Instrum. Methods **152**, 463 (1978).

[21] G. S. Bauer and R. Scherm, Physica **136B**, 80 (1986). A device of this kind has been tested by C. Majkrzak at Brookhaven National Laboratory (unpublished).

[22] G. M. Drabkin, Sov. Phys. JETP **11**, 724 (1960).

[23] Surface Science Laboratories, Inc., Mountain View, CA. The lithium glass (GS-20) was obtained from Reuter-Stokes, Twinsburg, OH.

[24] R. A. Schrack, Nucl. Instrum. Methods **222**, 499 (1984). Using a similar multichannel plate, Dr. Schrack obtained a resolution better than 1 mm.

[25] R. K. Crawford, R. T. Daly, J. R. Haumann, R. L. Hitterman, C. B. Morgan, G. E. Ostrowski, and T. G. Worlton, IEEE Trans. Nucl. Sci. **NS-28**, 3692 (1981).

[26] J. R. Haumann, R. T. Daly, T. G. Worlton, and R. K. Crawford, IEEE Trans. Nucl. Sci. **NS-29**, 62 (1982).

[27] Digital Equipment Corp., Maynard, MA.

[28] The Ealing Corp., South Natick, MA.

[29] L. Névot and P. Croce, Phys. Appl. **15**, 761 (1980).

[30] L. Névot, thesis, Paris-Sud, 1978 (unpublished).

[31] A. Steyerl, Z. Phys. **254**, 169 (1972).

[32] C. F. Majkrzak, J. D. Axe, and P. Böni, J. Appl. Phys. **57**, 3657 (1985).

[33] Obtained from Crystal Tec, Leti, Grenoble.

[34] K. Gray, R. Hilleke, R. Kampwirth, and G. P. Felcher (to be published).

[35] S. S. P. Parkin, J. K. Howard, R. Hilleke, and G. P. Felcher, Bull. Am. Phys. Soc. **31**, 225 (1986).